S. V. Fotin, A. P. Reeves, A. M. Biancardi, D. F. Yankelevitz, and C. I. Henschke. "Standard moments based vessel bifurcation filter for computer-aided detection of pulmonary nodules," In *Medical Imaging 2010: Computer-aided Diagnosis*, N. Karssemeijer, R. M. Summers, eds., vol. 7624, pp. 762413, 2010.

http://dx.doi.org/10.1117/12.844516

Standard moments based vessel bifurcation filter for computer-aided detection of pulmonary nodules

Sergei V. Fotin[a], Anthony P. Reeves[a], Alberto M. Biancardi[a]
David F. Yankelevitz[b] and Claudia I. Henschke[b]

[a]School of Electrical and Computer Engineering, Cornell University,
Ithaca, NY 14853, USA;
[b]Department of Radiology, NewYork-Presbyterian Hospital - Weill Cornell Medical Center,
New York, NY 10021, USA

ABSTRACT

This work describes a method that can discriminate between a solid pulmonary nodule and a pulmonary vessel bifurcation point at a given candidate location on a CT scan using the method of standard moments. The algorithm starts with the estimation of a spherical window around a nodule candidate center that best captures the local shape properties of the region. Then, given this window, the standard set of moments, invariant to rotation and scale is computed over the geometric representation of the region. Finally, a feature vector composed of the moment values is classified as either a nodule or a vessel bifurcation point.

The performance of this technique was evaluated on a dataset containing 276 intraparenchymal nodules and 276 selected vessel bifurcation points. The method resulted in 99% sensitivity and 80% specificity in identifying nodules, which makes this technique an efficient filter for false positives reduction. Its efficiency was further evaluated on the dataset of 656 low-dose chest CT scans. Inclusion of this filter into a design of an experimental detection system resulted in up to a 69% decrease in false positive rate in detection of intraparenchymal nodules with less than 1% loss in sensitivity.

Keywords: Automated pulmonary nodule detection, False positive reduction, Standard moments, Vessel bifurcations, Computer-assisted diagnosis (CAD), Computed tomography (CT).

1. INTRODUCTION

Achieving both high sensitivity and low false positive rate is the key purpose of an automated nodule detection system. While isolated intraparenchymal nodules with none or very few vascular attachments are easy to detect, lesions with significant attachments are often confused with blood vessels of different morphological variations. If the detection system is configured for high sensitivity, pulmonary vessel junction points become a significant source of false positive findings.[1–5]

There are several types of false positives caused by vessel junction points. The most common junction is a vessel bifurcation where a parent branch splits into two children branches of approximately equal and smaller diameters as illustrated in Figure 1(b). The morphology of such a junction is somewhat similar to a nodule attached to a vessel of comparable size shown in Figure 1(a) and, therefore, poses a challenge for an automated detection method. A second possible case is rarer and shown in Figure 2: one child branch could be much smaller while another one has roughly the same diameter and is collinear with the parent branch. The remaining large class of vascular structures contains more complex junctions and crossings of multiple branches. An example is given in Figure 3.

This particular work is focused on a method for the discrimination of true nodules from the most common class of vessel bifurcations. Even though the morphology of the vessel bifurcation is relatively straightforward, it is difficult to come up with a simple method that will robustly distinguish them from pulmonary nodules. Moreover, this type of junction point often occurs near the mediastinum region where the pulmonary vessels are

---

Send correspondence to Sergei V. Fotin, e-mail: svf3@cornell.edu, phone: 1 607 255 0963

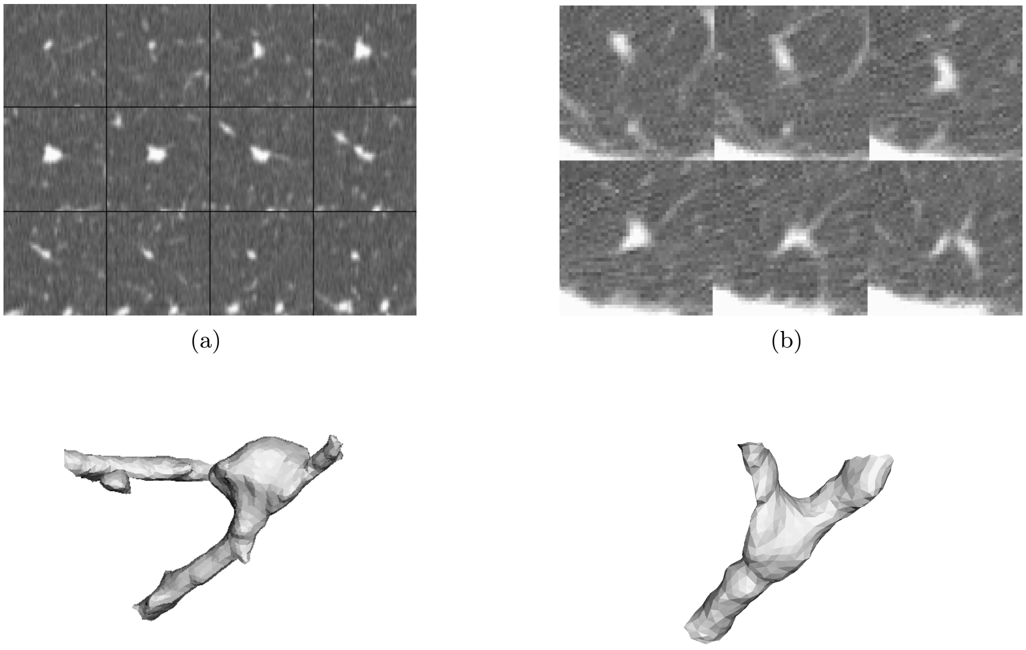

(a) (b)

(c) (d)

Figure 1. An example of typical candidate shapes to be discriminated: vascularized nodule (a) and pulmonary vessel bifurcation point (b). Light shaded 3D rendering after thresholding the images at the level of -400 HU are shown in subfigures (c) and (d).

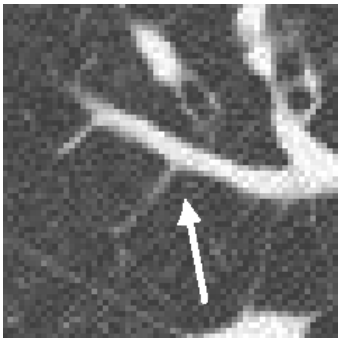

Figure 2. An example of a vessel bifurcation, showing unequally sized child branches.

affected by heart motion or pass close to the airway tree which complicates the discrimination. We believe that a series of methods that target a specific class of false positives will yield a better performance than the commonly used universal filters that target all possible false positive types at the same time.

While there has been much research on the discrimination of a broad class of false positives from nodules, surprisingly very little attention has been devoted to the particular classes of false positives and vessel bifurcations in particular. Zhao et al.[6] proposed a parametric model of the bifurcation point made of three toroidal components. Local principal curvatures were used to map a pixel to either a junction, a vessel or an ellipsoid nodule model with subsequent classification. Bahlmann et al.[7] used Gaussian model fitting followed by extraction of a manifold containing information on the bounding sphere and further analysis. Even though the technique looks promising, it has not been quantitatively evaluated. Several attempts were made to extract the entire pulmonary vasculature tree from a CT scan with the purpose of eliminating false positives caused by vessel junctions. The works of Croisille et al.[8] and Agam et al.[1] showed some improvement in false positive reduction, however, in addition to the high complexity of the method, the sensitivity of the detection suffered as well. Earlier work of our research group[2] employed a feature that assesses the extent of an attachment relative to a size of a candidate:

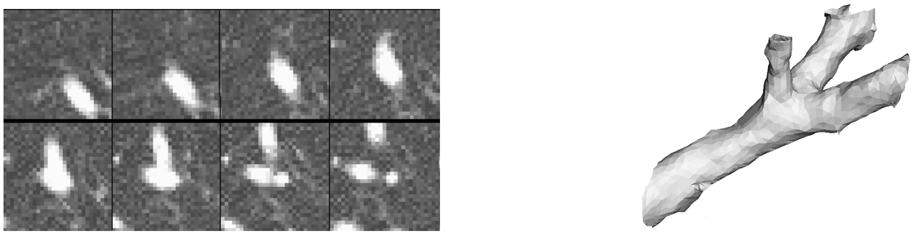

(a) (b)

Figure 3. An example of complex pulmonary vessel junction point: (a) montage view and (b) 3D rendering.

a vessel junction point would have less enclosed volume than a true nodule for the same amount of attachment. Another technique that was used for the discrimination of the vessel junctions is the analysis of the candidate's principal axes computed from moments. True round-shape nodules would have high compactness, or the low ratio of the largest to smallest axis of the ellipsoid of inertia. In contrast, the smallest axis of the bifurcation point region would be considerably smaller than the largest axis. All mentioned techniques had only limited success in the past.

2. METHOD

The method presented here does not seek to construct an explicit geometric model of a nodule or a bifurcation point, but rather to capture the difference between these two shapes from their geometric signatures. Since a round nodule and a vessel bifurcation are two fundamentally different objects, they must have different rotational properties and, consequently, distinct sets of moments. Size and orientation of the same class objects might be different within the class; therefore normalization is needed which is achieved by the method of three-dimensional standard moments. We hypothesize that standard moments provide a numerical characterization of an object shape that can be used to discriminate between true nodules and pulmonary vessel junctions.

Multiscale Laplacian of Gaussian (LoG) based detector identified nodule candidates from a whole-lung CT scan and supplied their centroids and radii.[9] Selection of a specific candidate generator is not important for presented method as long as it provides the approximate location of nodule candidates.

In this work, geometric moments (based on binary segmented image) were chosen over density moments (computed from the raw pixel values), since they have been better explored in the task of pattern classification. Geometric moments are different from density based moments by the fact that they are computed for binary images, where the intensity values are set either to one (foreground) or zero (background). Once the moments are computed, they can be used in characterization of the candidate shape.

In summary, provided that the nodule candidates are given, the main steps of the proposed algorithm are as follows:

1. Candidate subimage preprocessing.
    (a) resampling to isotropic space
    (b) intensity thresholding
    (c) bounding the candidate subregion with a sized sphere
2. Calculation of the standard moments set.
3. Classification of the moments vector.

These steps are discussed in detail further in the paper.

2.1 Candidate preprocessing

The preprocessing step starts with isotropic resampling of the candidate subregion to equalize the image resolution along the three coordinate axes.

The binary image $B(x, y, z)$ of the candidate was obtained by thresholding the candidate subregion of the isotropic image $I(x, y, z)$ using value of T:

$$B(x,y,z) = \begin{cases} 1, & \text{if } I(x,y,z) > T; \\ 0, & \text{otherwise.} \end{cases} \tag{1}$$

This threshold must separate the solid tissue from the surrounding parenchyma and provide the foreground region for the subsequent raw moments calculation.

In order to compute the set of raw moments, the region of interest $t(x, y, z)$ first must be selected to incorporate as much useful shape discrimination information as possible. This is achieved by imposing a spherical mask $S(R)$ of radius R centered over the candidate and rejecting all image data of the candidate subregion that is outside the mask:

$$t(x,y,z) = \begin{cases} B(x,y,z), & \text{if } (x,y,z) \in S(R); \\ 0, & \text{otherwise.} \end{cases} \tag{2}$$

Here the selection of radius R is important: if the radius is small relative to the extent of the candidate, the window will not contain any lung parenchyma and there will be no way of discriminating the shapes. Conversely, if the window is too large, it may contain other pulmonary structures that will negatively affect the calculation and introduce unnecessary noise. This radius should depend on the size of the candidate, but in the general case, we do not have such information. To address this issue, we introduce the concept of a foreground fraction $F(R)$, which is equal to the ratio of foreground volume to the total volume of a spherical mask $S(R)$.

$$F(R) = \frac{\sum\limits_{x,y,z \in S(R)} B(x,y,z)}{\sum\limits_{x,y,z \in S(R)} 1}. \tag{3}$$

The radius R of the spherical mask is the smallest one among those resulting in foreground fraction no greater than parameter P:

$$R = inf\Big\{r : F(r) \leq P\Big\}, \tag{4}$$

or, in other words, the spherical mask is selected such that the fraction of the foreground component inside approximately equals to P, the same for all candidates. An example of initial candidate subregion and the results of the preprocessing are shown in Figure 4. The optimal values for the parameters T and P were determined by experiment.

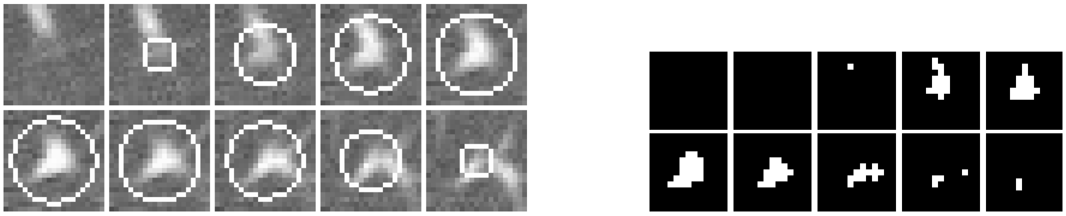
(a) (b)

Figure 4. An example of original candidate subregion showing the surface of the masking sphere (a); result of intensity thresholding and subregion masking (b).

2.2 Calculation of the standard moments set

The method of standard moments was first applied to the classification of three-dimensional shapes by Reeves and Wittner.[10] Standard moments have the advantage over the raw moments because they are normalized with respect to translation, rotation and scale transformation and remain invariant for a given object. They can be used in detection and characterization of objects that can be located anywhere within the space of interest, arbitrarily oriented and have different size.

Raw three-dimensional moments of order $p+q+r$ for the candidate region of interest $t(x,y,z)$ are defined by:

$$M_{pqr} = \sum_{x,y,z \in S(R)} x^p y^q z^r t(x,y,z). \tag{5}$$

Standard moments S_{pqr} can be directly computed from the raw moments by normalization. First, the volume of the object is scaled to be 1:

$$M'_{pqr} = \lambda^{3+p+q+r} M_{pqr},\ \lambda = \left(M_{000}\right)^{-\frac{1}{3}}. \tag{6}$$

Translation normalization is achieved by shifting the origin of the coordinate system to candidate's center of mass by the following transformation:

$$M''_{pqr} = \sum_{s=0}^{p} \sum_{t=0}^{q} \sum_{u=0}^{r} \binom{p}{s} \binom{q}{t} \binom{r}{u} a^{p-s} b^{q-t} c^{r-u} M'_{stu}, \tag{7}$$

where $a = -M'_{100}$, $b = -M'_{010}$, $c = -M'_{001}$.

Rotation normalization is done by aligning the candidate's principal axes with the coordinate axes:

$$\begin{aligned} S_{pqr} = M'''_{pqr} = &\sum_{s_1=0}^{p} \sum_{t_1=0}^{s_1} \sum_{s_2=0}^{q} \sum_{t_2=0}^{s_2} \sum_{s_3=0}^{r} \sum_{t_3=0}^{s_3} \binom{p}{s_1} \binom{s_1}{t_1} \binom{q}{s_2} \binom{s_2}{t_2} \binom{r}{s_3} \binom{s_3}{t_3} \cdot \\ &u_{11}^{t_1} u_{21}^{t_2} u_{12}^{s_1-t_1} u_{22}^{s_2-t_2} u_{13}^{p-s_1} u_{33}^{q-s_2} u_{31}^{t_3} u_{32}^{s_3-t_3} u_{33}^{r-s_3} \cdot M''_{t_1+t_2+t_3, s_1+s_2+s_3-t_1-t_2-t_3, p+q+r-s_1-s_2-s_3}, \end{aligned} \tag{8}$$

where $U = (u_{ij}) = (\pm u_1, u_2, u_3)^T$ is made of the orthonormal set of eigenvectors of the matrix N, which is, in turn, composed of the second order scaled and translated moments:

$$N = \begin{pmatrix} M''_{200} & M''_{110} & M''_{101} \\ M''_{110} & M''_{020} & M''_{011} \\ M''_{101} & M''_{011} & M''_{002} \end{pmatrix}. \tag{9}$$

The sign of u_1 is selected such that $det(U) = 1$. If $\{u_i\}$ are sorted in the order of descending eigenvalues, than the object's largest principal axis will be aligned along x and the smallest one along z coordinate axes without ambiguity. The standard set of moments up to order three $p+q+r \leq 3$ is computed. Some of the moment values are trivial and disregarded – the volume of the object after normalization is equal to 1: $S_{000} = 1$; the center of mass is at the origin of the coordinate system: $S_{100} = S_{010} = S_{001} = 0$; and the principal axes of the ellipsoid of inertia are lie on the coordinate axes: $S_{110} = S_{101} = S_{011} = 0$. Finally, the following set of remaining thirteen standard moment values is used in classification: S_{200}, S_{020}, S_{002}, S_{300}, S_{030}, S_{003}, S_{201}, S_{210}, S_{120}, S_{102}, S_{111}, S_{021}, S_{012}.

2.3 Classification of the moments vector

In the context of the high dimensionality of the feature vector, where the importance of each individual component is unknown, a soft margin support vector machine (SVM) with a polynomial kernel was chosen for classification. The SVM^{light} package[11] was used in the implementation.

3. EXPERIMENT

The evaluation set consisted of 276 intraparenchymal nodules with a diameter no less than 4 mm from the documented dataset of 656 low-dose whole-lung CT scans with the slice thickness of 1.25 mm obtained from Weill Cornell Medical Center. This dataset is maintained by our research group and was extensively used in the previous studies.[2,9,12] In our experimental setup the cases with an even case identifier were used for training and optimization, while the odd cases were used only for final testing. Accordingly, 130 nodules were used for training and 146 nodules for testing. In addition to true nodules, the same number of bifurcation points was manually sampled from the set of available candidates provided by our nodule candidate generator.

The discrimination scheme was optimized exclusively on the training set using five fold cross validation. The parameters to optimize were foreground volume fraction P and intensity threshold T. Since we are interested in the design of a false positive reduction filter, that would preserve all true nodules and filter out false candidates, we used the false positive reduction fraction obtained at 100% sensitivity to true nodules as the performance measure. For example, if a certain configuration of the filter reduced the number of vessel bifurcations from original 130 to 65 without the loss of sensitivity to true nodules, the corresponding reduction fraction would be equal to 0.5. The optimization was done jointly for the foreground volume fraction P and the threshold T. The configuration, incorporating the optimal parameters and classification model was applied to the test set and the resultant false positive reduction was obtained.

Once the optimal values for P and T were determined, the performance of the resulting classifier was compared to a previously developed techniques of (a) principal curvatures,[13,14] (b) ellipsoid of inertia compactness, and (c) attachment ratio.[2] The area under the Receiver Operating Characteristic (ROC) curve (AUC), obtained for the task of discrimination between nodules and vessel bifurcation points on the test set, was used as the performance metric.

Finally, the significance of the standard moments based filter was evaluated on the experimental nodule detection system previously developed by our research group. The free-response receiver operating characteristic (FROC) curves were generated for the test set before and after application of the filter. In addition, false positive reduction fractions were calculated at different levels of detection sensitivity.

Table 1. The values of false positive reduction fraction obtained for different foreground volume fractions and intensity thresholds on the training set.

		Foreground volume fraction P				
		0.1	0.2	0.3	0.4	0.5
Threshold T, HU	-250	0.43	0.61	0.08	0.06	0.01
	-300	0.47	0.68	0.30	0.11	0.02
	-350	0.36	0.71	0.54	0.20	0.13
	-400	0.29	0.69	**0.75**	0.28	0.17
	-450	0.28	0.64	0.63	0.28	0.18
	-500	0.27	0.61	0.51	0.32	0.22
	-550	0.27	0.43	0.42	0.37	0.27
	-600	0.17	0.42	0.42	0.31	0.18
	-650	0.16	0.34	0.39	0.30	0.15

4. RESULTS AND DISCUSSION

The results of the optimization on a training set with respect to the false positive reduction fraction are shown in Table 1. The values $P = 0.3$ and $T = -400HU$ that corresponded to the reduction fraction of 0.75 at 100% sensitivity were selected as optimal and applied to the test set. The resultant false positive reduction fraction on the test set was 0.80 at a sensitivity of 99%: one nodule out of 146 was rejected as the result of the filtering.

The resulting ROC of the model with optimal parameters is given in Figure 5 together with the classification performance of the other methods applied individually to the same test dataset. We see that the standard moments method resulted in a higher AUC of 0.99 compared to the conventional shape analysis techniques based on principal curvatures (AUC=0.89) and the ellipsoid of inertia (AUC=0.86). Moreover, the method provides better discrimination between nodules and bifurcation points than the attachment ratio feature (AUC=0.97), previously employed by our detection system. From the ROC plot we also can see that at very high sensitivity settings close to 100%, the standard moments based filter had the highest specificity among considered methods.

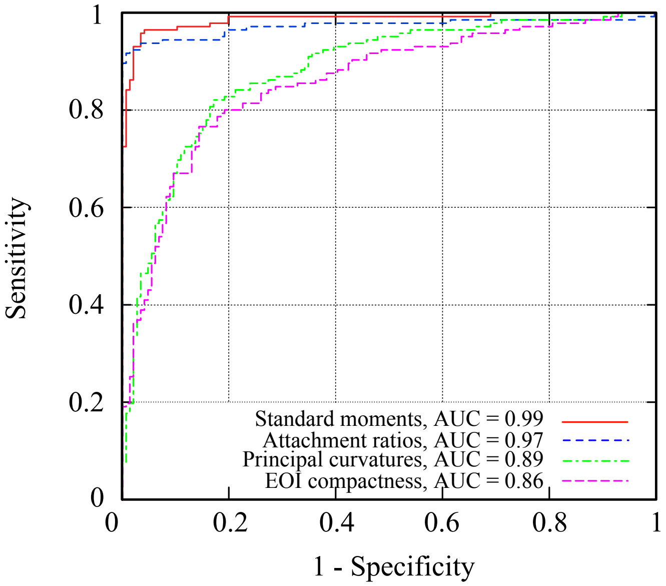

Figure 5. Performance of individual predictors for nodule - vessel bifurcation point discrimination on the test set.

A comparison of the FROC curves for the experimental detection system obtained with and without standard moments based filter is given in Figure 6. An alternative way to represent the change in the detection performance is shown in Figure 7. Here the values of false positive reduction fraction are given at different levels of detection sensitivity. From these graphs, we can observe that the standard moment method results in a significant reduction of the false positive rate especially at high detection sensitivity levels, where the pulmonary vessels are still very often confused with true nodules. However, at low sensitivity levels, the filters, previously used in the experimental detection system, are capable of rejecting vessel bifurcations. Consequently, the benefits of using this vessel bifurcation filter are very low for these sensitivity rates.

An example, where the standard moment method achieves an advantage over previously used techniques is shown in Figure 8. We observe how partial volume effect ”erodes” the thin branches of small bifurcation point, while the junction point remains. It makes the usage of attachment and ellipsoid of inertia filters inefficient. However, new filter was able to distinguish the geometry of branches and classify the example properly.

The example cases where the nodules and bifurcation points were missclassified by the moment filter are shown in Figure 9. Both cases have the geometric morphology different from typical representatives of the class: the bifurcation point in Figure 9(a) is adjacent to other pulmonary vessels, while the nodule in Figure 9(b) has unusual elongated shape with multiple vessel attachments.

5. CONCLUSION

A standard moments based vessel bifurcation filter for computer-aided detection of pulmonary nodules is presented and evaluated. The method resulted in 99% sensitivity and 80% specificity for the task of distinguishing nodules from vessel bifurcation points. Moreover, the filter was able to reject up to 69% of the false positives with almost no loss in sensitivity after incorporating it into design of an experimental detection system. These results suggest that the method of standard moments is very effective for rejecting bifurcation false positives for the task of automated nodule detection.

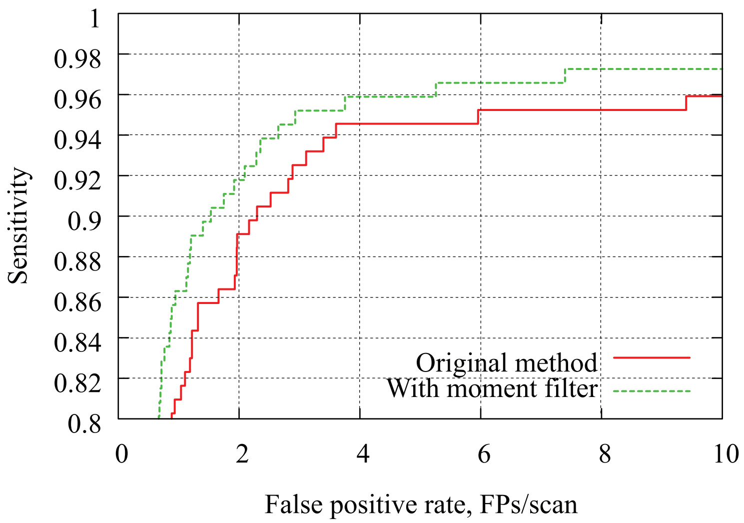

Figure 6. Performance of the moment-based filter in experimental detection system: FROC curves obtained with and without the standard moment based filter.

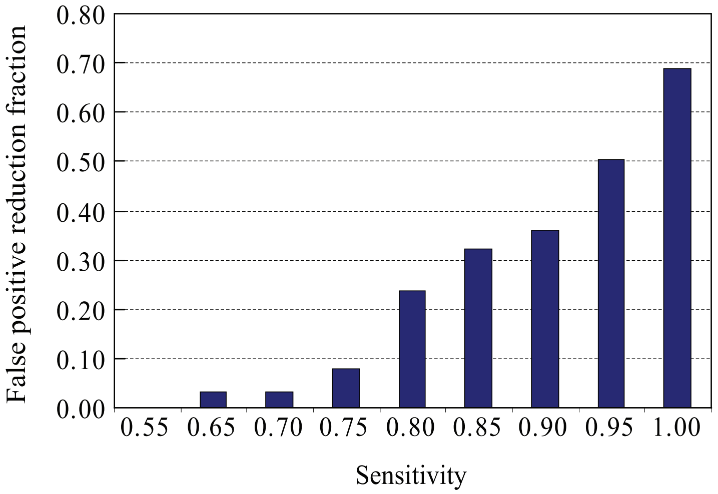

Figure 7. Performance of the moment-based filter in experimental detection system: false positive reduction fraction at different levels of sensitivity.

6. ACKNOWLEDGMENTS

This research was supported in part by NIH grant R33CA101110 and the Flight Attendants' Medical Research Institute. Dr. Yankelevitz and Dr. Reeves are co-inventors on patents and other pending patents relating to evaluation of diseases of the chest including measurement of nodules. Some of these, which are owned by Cornell Research Foundation (CRF) are non-exclusively licensed to General Electric and they receive royalties from CRF pursuant to Cornell policy, which in turn is consistent with the Bayh-Dole Act. Dr Henschke is a co-inventor on patents and other pending patents relating to evaluation of diseases of the chest including measurement of nodules, some of which are owned by Cornell Research Foundation (CRF) are non-exclusively licensed to General Electric, but has divested herself of all financial or other interests. Dr. Yankelevitz is an inventor on a pending patent owned by PneumRx related to biopsy needles, serves as a medical advisor to them, and holds an equity interest in PneumRx.

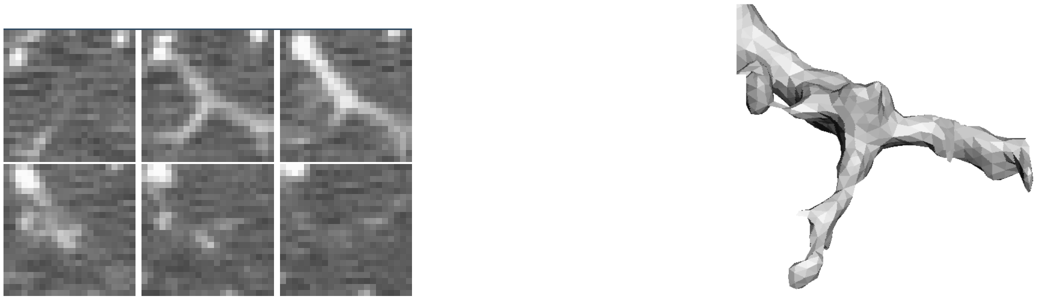
(a) (b)

Figure 8. An example of small bifurcation protruded due to partial volume effect. While it was correctly identified by the moment filter, it was confused with an attached nodule by both ellipsoid of inertia and attachment filters: montage view (a) and 3D rendering (b).

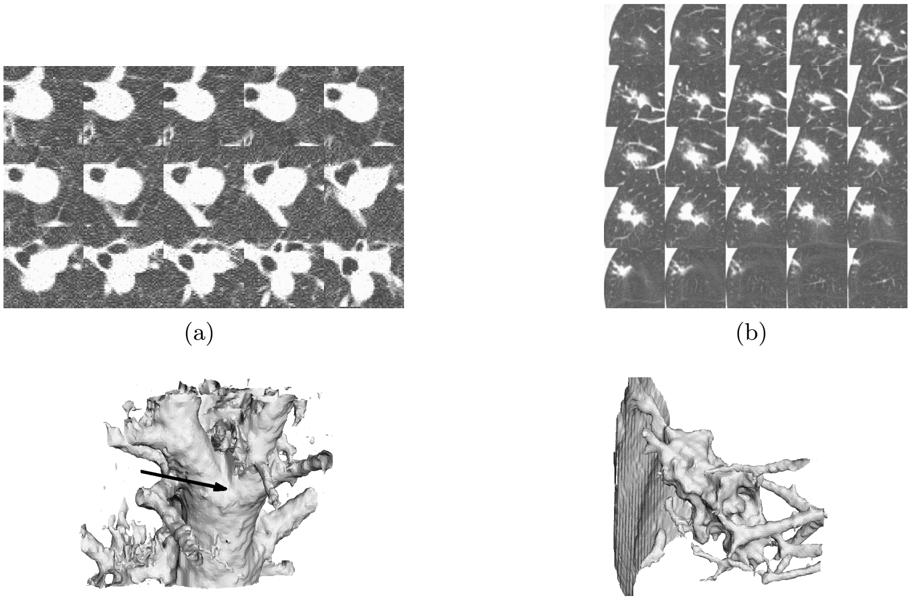
(a) (b)

(c) (d)

Figure 9. An example of incorrectly classified candidates: an axially oriented bifurcation point with multiple side attachments was identified as a nodule (a); a nodule of irregular shape was confused with a bifurcation point (b). Corresponding 3D visualizations are shown in subfigures (c) and (d).

REFERENCES

[1] Agam, G., Armato, S., and Changhua, W., "Vessel tree reconstruction in thoracic CT scans with application to nodule detection," *IEEE Transactions on Medical Imaging* **24**(4), 486– 499 (2005).

[2] Enquobahrie, A., Reeves, A. P., Yankelevitz, D. F., and Henschke, C. I., "Automated Detection of Small Solid Pulmonary Nodules in Whole Lung CT Scans from a Lung Cancer Screening Study," *Academic Radiology* **14**(5), 579–593 (2007).

[3] Das, M., Muhlenbruch, G., Mahnken, A., Flohr, T. G., and et al., "Small Pulmonary Nodules: Effect of Two Computer-aided Detection Systems on Radiologist Performance," *Radiology* **241**(2), 564 (2006).

[4] Pu, J., Zheng, B., Leader, J., Wang, X., and Gur, D., "An automated CT based lung nodule detection scheme using geometric analysis of signed distance field," *Medical Physics* **35**, 3453 (2008).

[5] Lee, Y., Tsai, D., Hara, T., Fujita, H., Itoh, S., and Ishigaki, T., "Improvement in automated detection of pulmonary nodules on helical x-ray CT images," in [*SPIE*], **5370**, 824–832 (2004).

[6] Zhao, F., Mendonça, P., Bhotika, R., and Miller, J., "Model-based junction detection with applications to lung nodule detection," *ISBI.(April 2007)* .

[7] Bahlmann, C., Li, X., and Okada, K., "Local pulmonary structure classification for computer-aided nodule detection," in [*Medical Imaging 2006: Image Processing. Edited by Reinhardt, Joseph M.; Pluim, Josien PW Proceedings of the SPIE*], **6144**, 1775–1785 (2006).

[8] Croisille, P., Souto, M., Cova, M., Wood, S., and et al., "Pulmonary nodules: improved detection with vascular segmentation and extraction with spiral CT. Work in progress," *Radiology* **197**(2), 397–401 (1995).

[9] Fotin, S. V., Reeves, A. P., Biancardi, A. M., Yankelevitz, D. F., and Henschke, C. I., "A multiscale Laplacian of Gaussian filtering approach to automated pulmonary nodule detection from whole-lung low-dose CT scans," in [*SPIE International Symposium on Medical Imaging*], **7260**, 72601Q (Feb 2009).

[10] Reeves, A. P. and Wittner, B. S., "Shape analysis of three dimensional objects using the method of moments," in [*IEEE Computer Society Conference on Computer Vision and Pattern Recognition*], 20–26 (1983).

[11] Joachims, T., "Making large-Scale SVM Learning Practical. Advances in Kernel Methods-Support Vector Learning, B. Schölkopf and C. Burges and A. Smola," (1999).

[12] Fotin, S. V., Reeves, A. P., Yankelevitz, D. F., and Henschke, C. I., "The impact of pulmonary nodule size estimation accuracy on the measured performance of automated nodule detection systems," in [*SPIE International Symposium on Medical Imaging*], 69151G (Feb 2008).

[13] Koenderink, J. J. and van Doorn, A. J., "Surface shape and curvature scales," *Image and Vision Computing* **10**(8), 557–565 (1992).

[14] Li, Q., Sone, S., and Doi, K., "Selective enhancement filters for nodules, vessels and airway walls in two- and three-dimensional CT scans," *Medical Physics* **30**(8), 2040–2051 (2003).